

See discussions, stats, and author profiles for this publication at: <https://www.researchgate.net/publication/6951588>

Electronic and Structural Evolution and Chemical Bonding in Tungsten Oxide Clusters: W_2O_n – and W_2O_n ($n = 1-6$)

ARTICLE *in* THE JOURNAL OF PHYSICAL CHEMISTRY A · AUGUST 2005

Impact Factor: 2.69 · DOI: 10.1021/jp051496f · Source: PubMed

CITATIONS

57

READS

40

6 AUTHORS, INCLUDING:



Jun Li

Tsinghua University

283 PUBLICATIONS 8,877 CITATIONS

SEE PROFILE



Lai-Sheng Wang

Brown University

429 PUBLICATIONS 18,551 CITATIONS

SEE PROFILE

Electronic and Structural Evolution and Chemical Bonding in Ditungsten Oxide Clusters: $W_2O_n^-$ and W_2O_n ($n = 1-6$)

Hua-Jin Zhai, Xin Huang, Li-Feng Cui, Xi Li, Jun Li, and Lai-Sheng Wang*

Department of Physics, Washington State University, 2710 University Drive, Richland, Washington 99352, and W. R. Wiley Environmental Molecular Sciences Laboratory, Pacific Northwest National Laboratory, MS K8-88, Post Office Box 999, Richland, Washington 99352

Received: March 22, 2005; In Final Form: May 4, 2005

We report a systematic and comprehensive investigation of the electronic structures and chemical bonding in a series of ditungsten oxide clusters, $W_2O_n^-$ and W_2O_n ($n = 1-6$), using anion photoelectron spectroscopy and density functional theory (DFT) calculations. Well-resolved photoelectron spectra were obtained at several photon energies (2.331, 3.496, 4.661, 6.424, and 7.866 eV), and W 5d-based spectral features were clearly observed and distinguished from O 2p-based features. More complicated spectral features were observed for the oxygen-deficient clusters because of the W 5d electrons. With increasing oxygen content in $W_2O_n^-$, the photoelectron spectra were observed to shift gradually to higher binding energies, accompanied by a decreasing number of W 5d-derived features. A behavior of sequential oxidation as a result of charge transfers from W to O was clearly observed. A large energy gap (2.8 eV) was observed in the spectrum of $W_2O_6^-$, indicating the high electronic stability of the stoichiometric W_2O_6 molecule. Extensive DFT calculations were carried out to search for the most stable structures of both the anion and neutral clusters. Time-dependent DFT method was used to compute the vertical detachment energies and compare to the experimental data. Molecular orbitals were used to analyze the chemical bonding in the ditungsten oxide clusters and to elucidate their electronic and structural evolution.

1. Introduction

Tungsten oxides are important materials with a variety of technological applications, such as in electrochromic devices,¹ as chemical sensors,^{2,3} and especially in heterogeneous catalysis.⁴⁻⁹ The basis for such a wide spectrum of applications is largely due to the variability of oxidation states, coordination environments, and degree of polymerization afforded by tungsten oxides. Gas-phase cluster studies have recently emerged as an alternative approach to obtain fundamental insight into the complicated structures and chemical processes in oxide materials and catalysis.¹⁰⁻²⁴ One of the major advantages of gas-phase studies is the ability to control the cluster stoichiometry. Clusters with essentially any compositions can be synthesized in the gas phase, ranging from the homonuclear metallic clusters to fully oxidized clusters, as well as oxygen-poor and oxygen-rich systems. The latter are particularly interesting because they are often the embodiment of bulk defects and may be used as molecular models for the bulk. Following our previous work on the monotungsten oxide clusters,²³ we study in the current work the ditungsten oxide clusters, W_2O_n and $W_2O_n^-$ ($n = 1-6$). We combine photoelectron spectroscopy (PES) and density functional theory (DFT) calculations to elucidate their chemical bonding and electronic and structural evolution.

There have been few previous studies on the $W_2O_n^-$ and W_2O_n ($n = 1-6$) clusters. Ackermann et al.²⁵ in 1963 conducted a thermodynamic study on tungsten oxide clusters and identified W_2O_6 , among others, as a thermodynamically important vapor species. Weltner et al.²⁶ performed a matrix infrared spectro-

scopic study on tungsten oxide clusters and tentatively assigned certain infrared bands to W_2O_6/W_3O_8 on the basis of their intensity variations with vaporization conditions. In a recent matrix infrared study, Andrews et al.²⁷ tentatively assigned an 832 cm^{-1} band to the W_2O_2 species. Ditungsten oxide cluster anions were produced using thermal desorption or laser vaporization techniques. However, only the $W_2O_6^-$ species was observed in typical mass spectra.^{28,29} Sun et al.³⁰ recently reported a photoelectron spectrum of $W_2O_6^-$ at 193 nm together with other stoichiometric $W_nO_{3n}^-$ ($n = 1, 3, 4$) clusters. They also presented optimized structures of neutral W_2O_n ($n = 1-6$) at the BPW91 level.

The current work is a continuation of our interest in oxide clusters.^{23,31-38} In particular, we recently reported a combined PES and ab initio and DFT study on monotungsten and monomolybdenum oxide clusters MO_n^- and MO_n ($M = W, Mo$; $n = 3-5$) and identified unique $W-O^\bullet$ and O_2^\bullet radical characters in WO_4 and WO_5 , respectively, which may have important implications in tungsten oxide catalysis.²³ In the present work, we report a combined PES and DFT study of a series of ditungsten oxide clusters: $W_2O_n^-$ and W_2O_n ($n = 1-6$). Extensive PES data were obtained at several photon energies (2.331, 3.496, 4.661, 6.424, and 7.866 eV), yielding a wealth of electronic information. A behavior of sequential oxidation was observed: with increasing oxygen content the low binding energy features primarily due to W 5d electrons were diminishing in numbers as a result of electron transfers from W to O. The PES spectra of $W_2O_6^-$ showed a large energy gap of 2.8 eV, characteristic of a stable stoichiometric W_2O_6 neutral molecule. Vibrational structures due to W–O stretching were resolved in several species ($\sim 810\text{ cm}^{-1}$ for W_2O , and $\sim 920\text{ cm}^{-1}$ for W_2O_3 , W_2O_4 , W_2O_5 , and W_2O_6). Extensive DFT

* E-mail: ls.wang@pnl.gov.

calculations were performed to optimize the geometric structures of both the anion and neutral clusters, to simulate the PES spectra, and to analyze the chemical bonding. The combined experimental and theoretical data allowed a comprehensive understanding of the electronic and structural evolution, chemical bonding, and sequential oxidation in the tungsten oxide clusters.

2. Experimental and Theoretical Methods

2.1. Photoelectron Spectroscopy. The experiments were carried out using a magnetic bottle PES apparatus equipped with a laser vaporization supersonic cluster source.^{39,40} Briefly, $W_mO_n^-$ cluster anions were produced by laser vaporization of a pure tungsten target in the presence of either pure helium carrier gas or helium carrier gas seeded with 0.5% O_2 and were analyzed using a time-of-flight mass spectrometer. The $W_2O_n^-$ ($n = 1-6$) series of clusters of current interest were each mass-selected and decelerated before being photodetached. Five detachment photon energies, either from a Nd:YAG laser or an ArF or F_2 excimer laser, were used in the current study: 532 nm (2.331 eV), 355 nm (3.496 eV), 266 nm (4.661 eV), 193 nm (6.424 eV), and 157 nm (7.866 eV). Photoelectrons were collected at nearly 100% efficiency by the magnetic bottle and analyzed in a 3.5-m-long electron flight tube. We found that the oxygen-deficient species, W_2O^- and $W_2O_2^-$, had very weak intensities with the O_2 -seeded helium carrier gas probably because of their high reactivity to form larger clusters. They were thus produced with pure helium carrier gas, where a trace amount of oxygen in the helium gas or residual oxygen contamination on the target surface served as a gentle oxygen source. Photoelectron spectra were calibrated using the known spectrum of Rh^- , and the energy resolution of the apparatus was $\Delta E_k/E_k \sim 2.5\%$, that is, ~ 25 meV for 1 eV electrons.

2.2. Density Functional Calculations. The theoretical calculations were performed at the DFT level using the B3LYP hybrid functional.⁴¹⁻⁴³ A large number of structural candidates were considered, and the search for the global minima and vibrational frequency calculations were performed using analytical gradients with the Stuttgart 14-valence electron pseudo-potentials and basis sets^{44,45} augmented with two f-type and g-type polarization functions ($\zeta_f = 0.256, 0.825$; $\zeta_g = 0.627$) for tungsten as recommended by Martin and Sundermann⁴⁶ and the aug-cc-pVTZ basis set for oxygen.^{47,48} Scalar relativistic effects, that is, the mass velocity and Darwin effects, were taken into account via the quasi-relativistic pseudo-potentials. Since we were mainly interested in explaining the experimental PES spectra, spin-orbit coupling effects were neglected. Our previous study on tungsten oxide species showed that spin-orbit coupling effects would shift the orbital energies by up to a few tenths of an eV,⁴⁹ which would not affect the spectral assignments. Only a selected set of optimized structures (the ground state and a few low-lying isomers), considered to be important in interpreting the experimental data, are reported. The vertical detachment energies (VDEs) were calculated using a combined Δ SCF-TDDFT approach previously outlined by us.^{50,51} In this approach, the ground-state energies of the anions and the neutrals were calculated from the Δ SCF energy difference at the B3LYP level, whereas the excited states of the electron-detached species were obtained from the TDDFT calculations of the neutrals. For all calculations, the extra fine integration grid was used to obtain highly accurate DFT results. All calculations were accomplished using the NWChem 4.6 program and the Molecular Science Computing Facility located at the Environmental Molecular Sciences Laboratory.⁵² The Extensible

TABLE 1: Measured Electron Affinities (EA) and Ground-State W–O Stretching Vibrational Frequencies for W_2O_n ($n = 1-6$) from Anion Photoelectron Spectra^a

	W_2O	W_2O_2	W_2O_3	W_2O_4	W_2O_5	W_2O_6
EA (eV)	1.58 (3)	1.77 (3)	2.22 (3)	3.08 (3)	3.60 (3)	3.52 (2)
vib (cm^{-1})	810 (40)		920 (50)	920 (40)	920 (40)	920 (40)

^a Numbers in the parentheses represent uncertainties in the last digits.

Computational Chemistry Environment (Ecce) software was used to generate the three-dimensional contours of the calculated Kahn–Sham orbitals.⁵³

3. Experimental Results

The PES spectra of $W_2O_n^-$ ($n = 1-6$) are shown in Figures 1–6, respectively, at various photon energies. The higher photon energies used in the current work allowed higher binding energy features to be observed, whereas the lower photon energies allowed the lower binding energy electronic transitions to be better resolved. The observed detachment transitions are labeled with letters and the vertical lines represent the resolved vibrational structures. A set of PES spectra for the whole $W_2O_n^-$ series are shown in Figure 7 to illustrate the spectral evolution and are compared to the simulated spectra, as will be discussed later. The obtained adiabatic detachment energies (ADEs), that is, the electron affinities (EAs) of the neutral clusters, and vibrational frequencies are given in Table 1. All the observed VDEs are given in Table 2 along with the theoretical results to be discussed later.

3.1. W_2O^- . The spectra of W_2O^- are shown at three photon energies in Figure 1. The 532-nm spectrum (Figure 1a) reveals two bands, both of which are vibrationally resolved. The vibrational structures in band X yield a vibrational frequency of 810 cm^{-1} for the ground state of W_2O neutral, likely due to the W–O stretching. However, the peak width for the 0–0 transition (~ 70 meV) of band X at 1.61 eV is much broader than the instrumental resolution, suggesting that other low-frequency modes are also involved. An ADE of 1.58 eV is obtained from the leading edge of the X band, which defines the EA of the neutral W_2O . Band A with a VDE of 2.06 eV represents the first excited state of W_2O neutral. It is also partially vibrationally resolved with a spacing of $\sim 800\text{ cm}^{-1}$. In the 355-nm spectrum (Figure 1b), a sharp peak B is observed at 2.25 eV, beyond which the spectrum becomes very congested. A broad band C centered around 2.68 eV with many overlapping features is observed, which is shown more clearly in the 266-nm spectrum (Figure 1c). The 266-nm spectrum shows continuous transitions at the higher binding energy side with broad bands D and E and a prominent feature F centered around 4.16 eV.

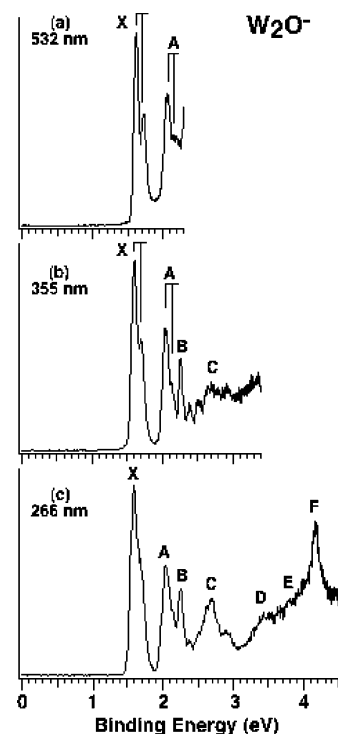
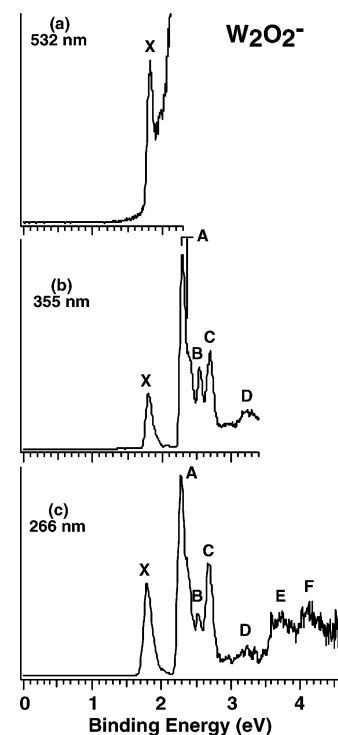
3.2. $W_2O_2^-$. The spectra of $W_2O_2^-$ are shown in Figure 2 at three photon energies. The 532-nm spectrum reveals only the ground-state transition X at a VDE of 1.81 eV. A huge tail is observed at the high binding energy side because of thermionic emissions,^{54,55} likely caused by the high photon flux used at 532 nm. Since no vibrational structures are resolved, the ADE is evaluated by drawing a straight line at the leading edge of feature X and then adding the instrumental resolution to the intersection with the binding energy axis. The ADE thus obtained is 1.77 eV, which also represents the EA of W_2O_2 neutral. The VDE of the X band is measured to be 1.81 eV from the peak maximum. The difference between the ADE and VDE implies that the peak X contains low-frequency vibrations. The 355-nm spectrum (Figure 2b) is well-resolved with several sharp and intense features (A, B, C) and a weak, broad feature

TABLE 2: Experimental Vertical Detachment Energies (VDE) from the Photoelectron Spectra of $W_2O_n^-$ ($n = 1-6$) and Comparison with Theoretical VDEs from Density Functional Calculations

		expt ^a		theor ^{b-d}			
		observed feature	VDE (eV)	MO	VDE (eV)	MO	VDE (eV)
W_2O^-	X	1.61 (2)	14a' (β)	1.24 (T)			
	A	2.06 (3)			14a' (α)	1.63 (S)	
	B	2.25 (3)			5a'' (α)	1.78 (S)	
	C	2.68 (5)	13a' (β)	2.11 (T)			
	D	~3.4	12a' (β)	2.81 (T)	13a' (α)	2.60 (S)	
	E	~3.8	4a'' (β)	3.47 (T)	12a' (α)	3.68 (S)	
$W_2O_2^-$	F	4.16 (5)	11a' (β)	3.90 (T)	4a'' (α)	3.94 (S)	
					11a' (α)	4.34 (S)	
	X	1.81 (3)			9b _u (α)	2.04 (S)	
	A	2.29 (3)	8b _u (β)	2.30 (T)			
	B	2.54 (2)			8b _u (α)	2.84 (S)	
	C	2.69 (2)	9a _g (β)	2.88 (T)			
$W_2O_3^-$	D	~3.2					
	E	~3.7	3a _u (β)	3.80 (T)			
	F	~4.2			9a _g (α)	4.16 (S)	
					3a _u (α)	4.22 (S)	
	X	2.25 (3)			9b ₁ (α)	2.50 (S)	
	A	2.88 (3)	12a ₁ (β)	3.03 (T)			
$W_2O_4^-$	B	3.7 (1)	4b ₂ (β)	3.65 (T)			
	C	4.3 (1)			12a ₁ (α)	4.26 (S)	
					4b ₂ (α)	3.95 (S)	
	D	4.78 (5)	11a ₁ (β)	4.66 (T)	11a ₁ (α)	4.91 (S)	
	E	5.98 (3)	8b ₁ (β)	5.74 (T)	8b ₁ (α)	5.89 (S)	
	F	~6.4	3b ₂ (β)	6.24 (T)	3b ₂ (α)	6.36 (S)	
$W_2O_5^-$			10a ₁ (β)	6.23 (T)	10a ₁ (α)	6.31 (S)	
	X	3.13 (2)			32a (α)	3.23 (T)	
	A	3.90 (5)			31a (α)	4.33 (T)	
	B	4.20 (5)			30a (α)	4.59 (T)	
	C	~5.0			29 (α)	~5.0 (T)	
	D	~6.0	28a (β)	6.02 (Q)	28a (α)	6.09 (T)	
$W_2O_6^-$	E	~6.8	27a (β)	6.58 (Q)	27a (α)	6.71 (T)	
	F	~7.2	26a (β)	6.77 (Q)	26a (α)	6.90 (T)	
	G	~7.7	25a (β)	7.06 (Q)	25a (α)	7.23 (T)	
	X	3.66 (3)			10b ₂ (α)	3.88 (S)	
	A	4.79 (3)	12a ₁ (β)	4.73 (T)			
	B	6.45 (3)	6a ₂ (β)	6.51 (T)	12a ₁ (α)	6.66 (S)	
$W_2O_7^-$			7b ₁ (β)	6.56 (T)	6a ₂ (α)	6.56 (S)	
					7b ₁ (α)	6.61 (S)	
	C	7.00 (3)	9b ₂ (β)	7.06 (T)	9b ₂ (α)	7.25 (S)	
			11a ₁ (β)	7.13 (T)	11a ₁ (α)	7.34 (S)	
	D	7.23 (3)	6b ₁ (β)	7.45 (T)	6b ₁ (α)	7.54 (S)	
	E	~7.5	8b ₂ (β)	7.51 (T)	8b ₂ (α)	7.81 (S)	
$W_2O_8^-$			10a ₁ (β)	7.66 (T)	10a ₁ (α)	7.82 (S)	
	X	3.63 (2)			17a ₁ (α)	3.71 (S)	
	A	6.57 (5)	11b ₂ (β)	6.43 (T)	11b ₂ (α)	6.47 (S)	
	B	6.95 (5)	10b ₂ (β)	6.71 (T)	10b ₂ (α)	6.80 (S)	
			8b ₁ (β)	6.90 (T)			
	C	7.29 (3)	3a ₂ (β)	7.12 (T)	8b ₁ (α)	7.16 (S)	
$W_2O_9^-$			16a ₁ (β)	7.08 (T)	16a ₁ (α)	7.22 (S)	
	D	7.59 (3)	7b ₁ (β)	7.40 (T)	3a ₂ (α)	7.44 (S)	
					7b ₁ (α)	7.59 (S)	

^a Numbers in the parentheses represent experimental uncertainty in the last digits. ^b On the basis of the anion ground-state structures as shown in Figures 8–12. ^c The ground-state electronic configurations for the anions are W_2O^- : $(11a')^2(4a'')^2(12a')^2(13a')^2(5a'')^1(14a')^2$; $W_2O_2^-$: $(7a_2)^2(2a_u)^2(8a_g)^2(3a_u)^2(9a_g)^2(8b_u)^2(9b_u)^1$; $W_2O_3^-$: $(10a_1)^2(3b_2)^2(8b_1)^2(11a_1)^2(4b_2)^2(12a_1)^2(9b_1)^1$; $W_2O_4^-$: $(25a)^2(26a)^2(27a)^2(28a)^2(29a)^2(30a)^1(31a)^1(32a)^1$; $W_2O_5^-$: $(10a_1)^2(8b_2)^2(6b_1)^2(11a_1)^2(9b_2)^2(7b_1)^2(6a_2)^2(12a_1)^2(10b_2)^1$; $W_2O_6^-$: $(7b_1)^2(16a_1)^2(3a_2)^2(8b_1)^2(10b_2)^2(11b_2)^2(17a_1)^1$. ^d The labels “ α ” and “ β ” denote majority and minority spins, whereas “S”, “T”, and “Q” denote singlet, triplet, and quintet W_2O_n final states upon photodetachment.

at the higher binding energy side (D, ~3.2 eV). The band A with a VDE of 2.29 eV represents the first excited state of the W_2O_2 neutral, defining an energy gap of 0.48 eV. The spectral pattern, that is, a relatively weak ground-state peak followed

**Figure 1.** Photoelectron spectra of W_2O^- at (a) 532 nm (2.331 eV), (b) 355 nm (3.496 eV), and (c) 266 nm (4.661 eV). The vertical lines represent the resolved vibrational structures.**Figure 2.** Photoelectron spectra of $W_2O_2^-$ at (a) 532 nm, (b) 355 nm, and (c) 266 nm.

by an energy gap and an intense band (Figure 2b, c), suggests that neutral W_2O_2 is a closed-shell molecule. Vibrational structure is tentatively assigned to band A with a frequency of ~800 cm^{-1} similar to those observed for W_2O (Figure 1). Bands B and C are observed at 2.54 and 2.69 eV, respectively. The 266-nm spectrum (Figure 2c) only reveals two very broad bands at ~3.7 eV (E) and ~4.2 eV (F).

3.3. $W_2O_3^-$. The spectra of $W_2O_3^-$ were taken at four photon energies, as shown in Figure 3. The 355-nm spectrum (Figure

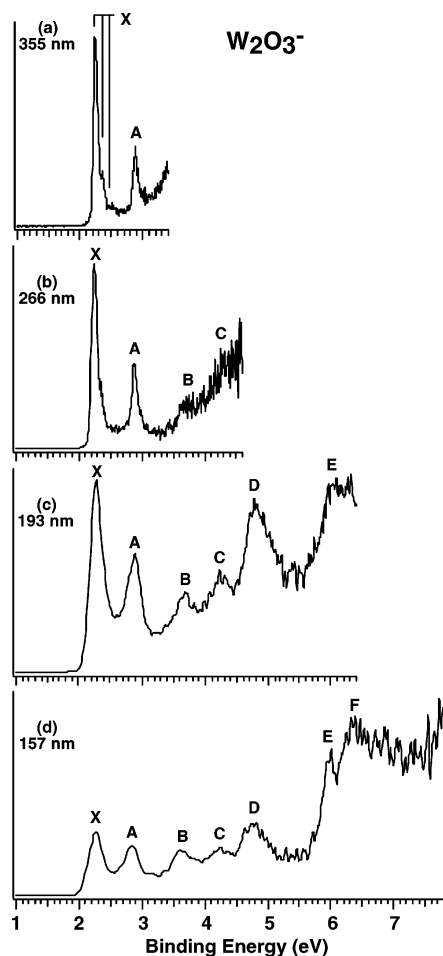


Figure 3. Photoelectron spectra of $W_2O_3^-$ at (a) 355 nm, (b) 266 nm, (c) 193 nm (6.424 eV), and (d) 157 nm (7.866 eV).

3a) reveals two sharp bands (X and A). The ground-state band X is intense with tentative vibrational structures and a spacing of 920 cm^{-1} . The 0–0 peak at 2.25 eV is again broader than the instrumental resolution, similar to the X band in the 532-nm spectrum of W_2O^- (Figure 1a). An ADE of 2.22 eV is obtained from the leading edge of this peak, which represents the EA of W_2O_3 neutral. Band A with a VDE of 2.88 eV is very sharp but appears to be weaker. The 266-nm spectrum (Figure 3b) reveals two more broad bands (B and C), which are observed more clearly in the 193- and 157-nm spectra. Two more broad bands (D and E) are observed at the higher binding energies in the 193-nm spectrum (Figure 2c). Band E becomes better defined in the 157-nm spectrum, but beyond 6.0 eV broad and continuous spectral features are observed (Figure 3d).

3.4. $W_2O_4^-$. The spectra of $W_2O_4^-$ at four photon energies are shown in Figure 4. The 355-nm spectrum (Figure 4a) reveals only the ground-state transition X, which is vibrationally resolved with a spacing of 920 cm^{-1} . The 0–0 transition at 3.13 eV is again broader than the instrumental resolution. Its leading edge yields an EA of 3.08 eV for neutral W_2O_4 . At 266 nm, two additional broad bands are observed at 3.90 eV (A) and 4.20 eV (B). A very weak band C at around 5.0 eV is observed in the 193-nm spectrum (Figure 4c), but the higher binding energy part is very congested and only becomes better defined in the 157-nm spectrum (Figure 4d), where four broad features (D, E, F, G) can be tentatively identified.

3.5. $W_2O_5^-$. The electron binding energies of $W_2O_5^-$ appear to be rather high and can be accessed only with 266-, 193-, and 157-nm photons (Figure 5). The 266-nm spectrum reveals

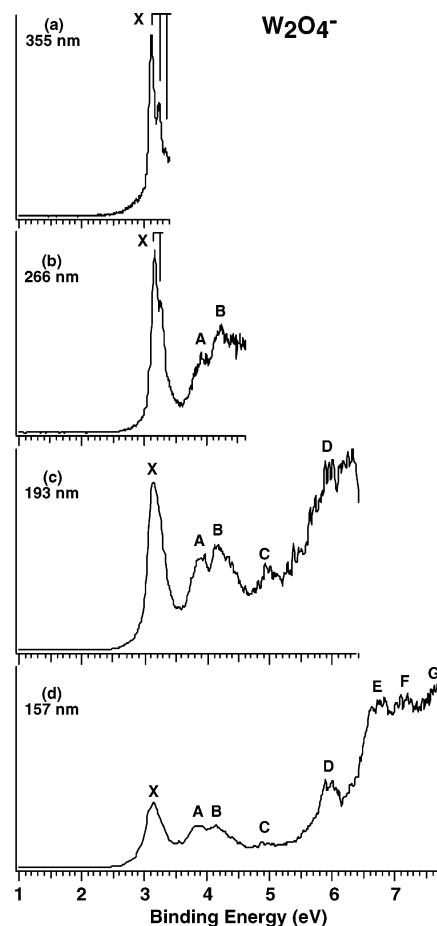


Figure 4. Photoelectron spectra of $W_2O_4^-$ at (a) 355 nm, (b) 266 nm, (c) 193 nm, and (d) 157 nm.

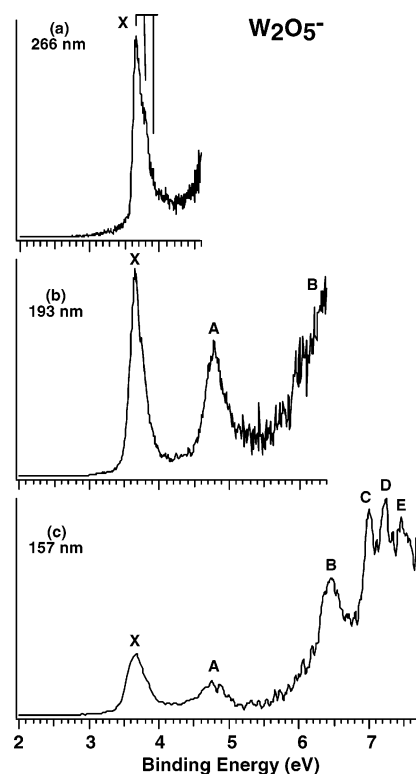


Figure 5. Photoelectron spectra of $W_2O_5^-$ at (a) 266 nm, (b) 193 nm, and (c) 157 nm.

only the ground-state transition X, which shows a tentative vibrational progression with a spacing of 920 cm^{-1} . Again, the

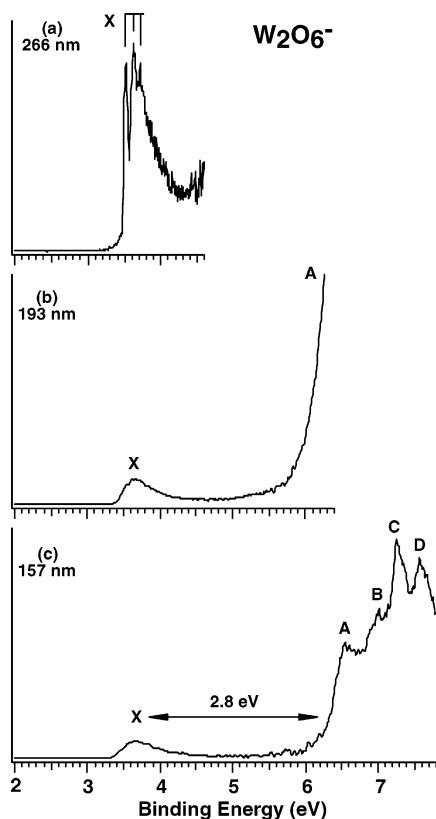


Figure 6. Photoelectron spectra of W_2O_6^- at (a) 266 nm, (b) 193 nm, and (c) 157 nm. The large X–A energy gap is denoted.

peak width here is much broader than the instrumental resolution, suggesting low-frequency vibrations. An ADE of 3.60 eV is obtained from the leading edge of band X, which also represents the EA of W_2O_5 neutral. The first excited state of W_2O_5 (band A) observed with a VDE of 4.79 eV in the 193-nm spectrum is quite broad (Figure 5b). Several transitions (B, C, D, E) are observed at very high binding energies in the 157-nm spectrum (Figure 5c).

3.6. W_2O_6^- . The spectra of W_2O_6^- at three photon energies (266, 193, and 157 nm) are shown in Figure 6. The 266-nm spectrum (Figure 6a) reveals the vibrationally resolved ground state (X) with a spacing of 920 cm^{-1} . The vibrational structure does not seem to be a simple vibrational progression, suggesting that there may be more than one active mode. The VDE is defined by the $1 \leftarrow 0$ transition at 3.63 eV. The $0 \leftarrow 0$ transition at 3.52 eV is very sharp and defines the ADE, as well as the EA of the W_2O_6 neutral. The first excited state (A) of W_2O_6 turns out to be barely accessible even at 193 nm (Figure 6b), which shows a large energy gap followed by a large tail on the high binding energy side. The 157-nm spectrum (Figure 6c) clearly shows the X–A gap (2.8 eV) and also reveals several higher binding energy features (B, C, D). The PES spectral pattern of W_2O_6^- is characteristic of a stable, closed-shell W_2O_6 neutral molecule with a large HOMO–LUMO gap (2.8 eV), consistent with the fact that W_2O_6 is a stable stoichiometric molecule. Sun et al.³⁰ recently reported a PES spectrum of W_2O_6^- at 193 nm, which is consistent with the current 193-nm data. However, the current vibrationally resolved data at 355 nm allow a more accurate EA (3.52 eV) to be measured for W_2O_6 , whereas the 157-nm data yield the true HOMO–LUMO gap (2.8 eV), compared to an ADE (3.40 eV) and HOMO–LUMO gap (2.5 eV) obtained from the 193-nm spectrum by Sun et al.

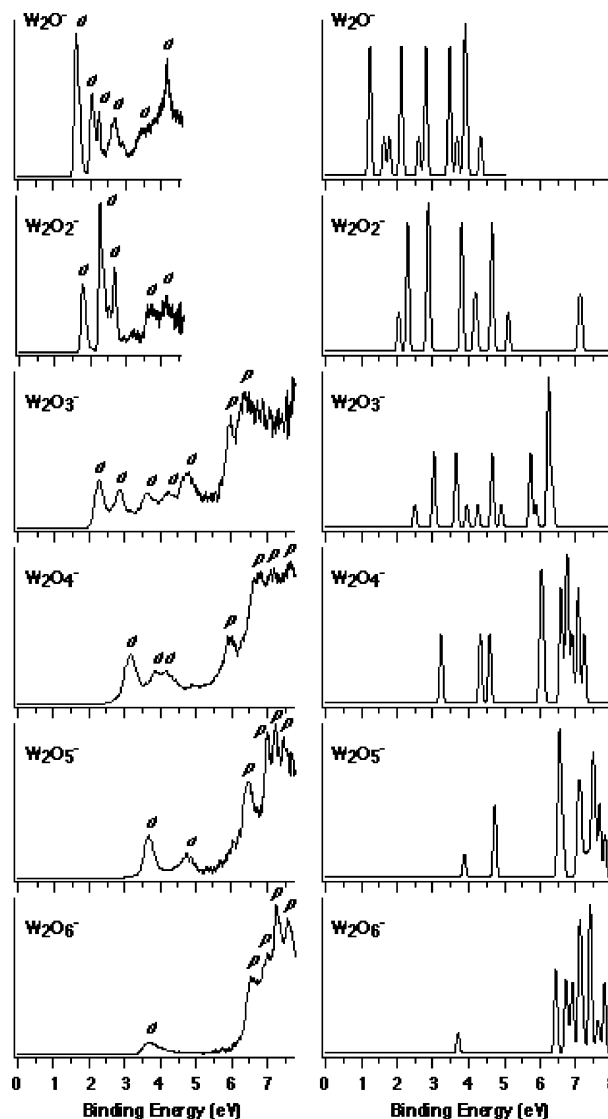


Figure 7. Comparison of experimental (left column) and simulated (right column) photoelectron spectra of W_2O_n^- ($n = 1\text{--}6$). The photoelectron features are denoted as “d” or “p” to indicate photo-detachment transitions from W 5d or oxygen 2p type orbitals. The simulated spectra were based on the optimized anion ground-state structures (Figures 8–12) and were constructed by fitting the distribution of the calculated vertical detachment energies (Table 2) with unit-area Gaussian functions of 0.04 eV full width at half-maximum.

4. Theoretical Results

Optimized ground-state geometries of W_2O_n and W_2O_n^- ($n = 1\text{--}6$) and selected low-lying isomers are presented in Figures 8–12.

4.1. W_2O and W_2O^- . The optimized structures of W_2O and W_2O^- are shown in Figure 8. Our calculations indicate that the ground state of neutral W_2O is open-shell ($^3A''$) with C_s symmetry, in which the O atom is bonded only to one W atom (Figure 8a). This result agrees with that identified by Sun et al.³⁰ at BPW91 level. The W–O and W–W bond lengths and the $\angle\text{WWO}$ bond angle are 1.722 Å, 2.256 Å, and 100.5° , respectively. The corresponding singlet state C_s ($^1A'$) is 0.95 eV higher in energy (Figure 8a). The triangular structures C_{2v} (3B_2) and C_{2v} (1A_1) are located 0.59 and 0.69 eV above the ground state, respectively (Figure 8b). The ground state of W_2O^- is $^2A''$ with C_s symmetry (Figure 8c) and there are no significant differences in geometry between the anion and neutral ground

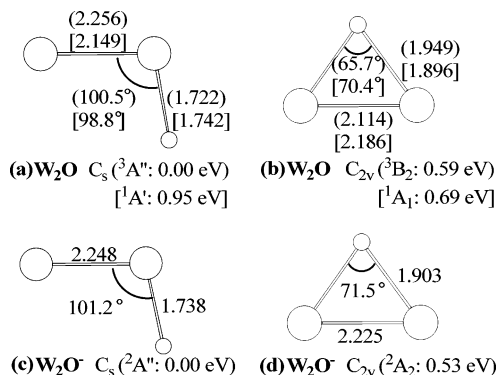


Figure 8. Optimized structures and their relative energies for W_2O and W_2O^- . The bond lengths are in Å.

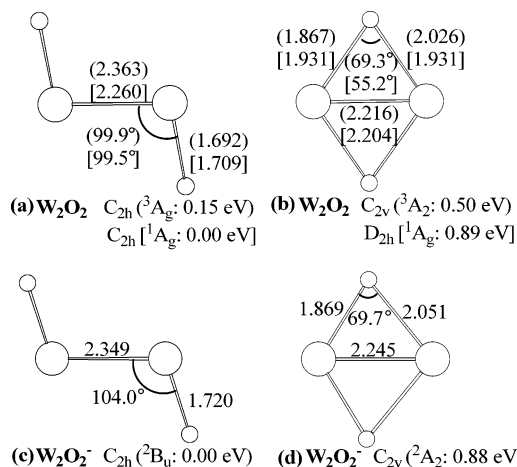


Figure 9. Optimized structures and their relative energies for W_2O_2 and W_2O_2^- . The bond lengths are in Å.

states. The triangular C_{2v} (2A_2) structure of W_2O^- is 0.53 eV higher in energy (Figure 8d).

4.2. W_2O_2 and W_2O_2^- . Many structures were studied in search of the ground states for W_2O_2 and W_2O_2^- . The ground state of neutral W_2O_2 is closed-shell (1A_g) with C_{2h} symmetry (Figure 9a), and it is related to the ground-state structure of W_2O . This structure is in agreement with that identified by Sun et al.³⁰ The corresponding triplet state C_{2h} (3A_g) of W_2O_2 is 0.15 eV higher in energy (Figure 9a), which differs from the ground state mainly in the W–W distance. The singlet and triplet dibridged rhombus structures, D_{2h} (1A_g) and C_{2v} (3A_2), are located 0.89 and 0.50 eV above the ground state, respectively (Figure 9b). The ground state of W_2O_2^- is 2B_u with C_{2h} symmetry (Figure 9c), very similar to the ground state of neutral W_2O_2 . The dibridged structure, C_{2v} (2A_2), for W_2O_2^- is 0.88 eV higher in energy (Figure 9d).

4.3. W_2O_3 and W_2O_3^- . The potential energy surfaces for W_2O_3 were rather flat with several closely lying isomers near the global minimum. The singly bridged structure is the most likely candidate for the global minimum. The identified ground state for W_2O_3 at the current level of theory is the planar C_{2v} (1A_1) structure (Figure 10a), which agrees with that found by Sun et al.³⁰ We also located a low-lying open-shell C_s ($^3A''$) structure for W_2O_3 (Figure 10b), which has similar interatomic connectivity to the C_{2v} (1A_1) ground state, but the bridging oxygen atom is substantially out-of-plane with a dihedral angle of 145.6°. This nonplanar structure is only 0.03 eV higher in energy. The singly bridged structures C_2 (1A) and C_2 (3B), in which the two terminal oxygen atoms are trans to each other, are located 0.07 and 0.38 eV above the ground state, respectively

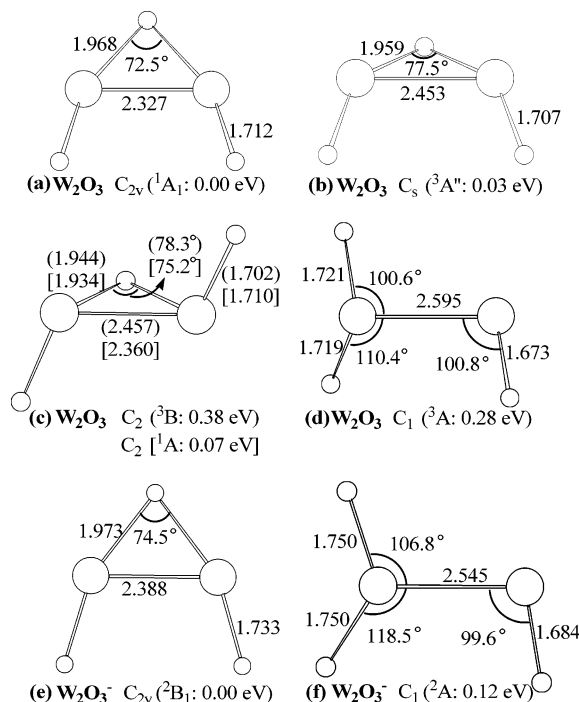


Figure 10. Optimized structures and their relative energies for W_2O_3 and W_2O_3^- . The bond lengths are in Å.

(Figure 10c). A C_1 (3A) structure without a bridging oxygen atom is 0.28 eV above the ground state (Figure 10d). The ground state of W_2O_3^- is the planar C_{2v} (2B_1) structure (Figure 10e), very similar to the ground state of neutral W_2O_3 (Figure 10a). The C_1 (2A) structure without a bridging O atom is a low-lying isomer slightly higher in energy by 0.12 eV (Figure 10f). A dibridged structure of W_2O_3^- was found to be 1 eV less stable than the singly bridged one (not shown).

4.4. W_2O_4 and W_2O_4^- . An extensive search of the potential energy surfaces of W_2O_4 and W_2O_4^- resulted in several low-lying isomers, as shown in Figure 11. The ground state of neutral W_2O_4 is C_1 (3A), which is based on the four-membered-ring W_2O_2 rhombus with the W atoms each terminally attached by an extra oxygen atom (Figure 11a). The two bridging oxygen atoms are closer to one tungsten atom than the other by about 0.2 Å, which implies that neutral W_2O_4 may be viewed as a WO_3 unit interacting with a $\text{W}=\text{O}$ unit. Consequently, the tungsten atom in the $\text{W}=\text{O}$ unit has two unpaired electrons (see below and Figure 16a). This ground-state structure is basically in agreement with that identified by Sun et al.,³⁰ except that the structure of Sun et al. possesses higher symmetry (C_{2v}). In our current calculations, such a C_{2v} structure (not shown) is 0.23 eV higher in energy and represents a saddle point. However, a mono-oxygen bridged structure (Figure 11b) is nearly degenerate with the dibridged structure and is only higher in energy by 0.08 eV in the current level of theory. Among other structures optimized for W_2O_4 , the dibridged singlet state C_1 (1A) (Figure 11d) and the monobridged singlet C_1 (1A) structure (Figure 10c) were located 0.81 and 0.51 eV above the ground state, respectively. The ground state of W_2O_4^- is the monobridged C_1 (4A) structure (Figure 11e). The corresponding doublet C_1 (2A) state is 0.18 eV higher in energy (Figure 11f). The dibridged quartet state C_1 (4A) and doublet state C_1 (2A) are 0.27 and 0.65 eV above the ground state, respectively (Figure 11g and h).

4.5. W_2O_5 and W_2O_5^- . The ground state of W_2O_5 neutral is C_s ($^1A'$) (Figure 12a), which is related to the ground-state structure of W_2O_4 . One W atom is bonded to two terminal O

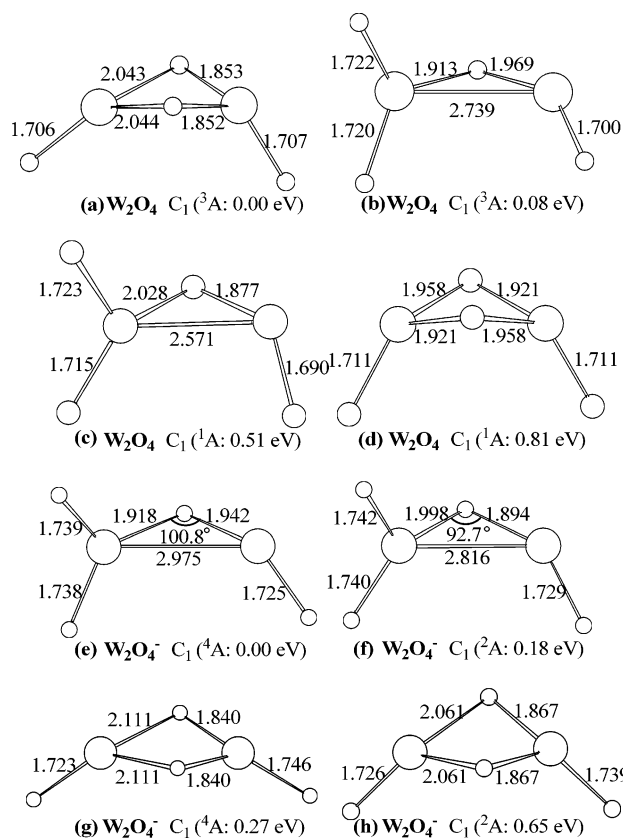


Figure 11. Optimized structures and their relative energies for W_2O_4 and W_2O_4^- . The bond lengths are in Å.

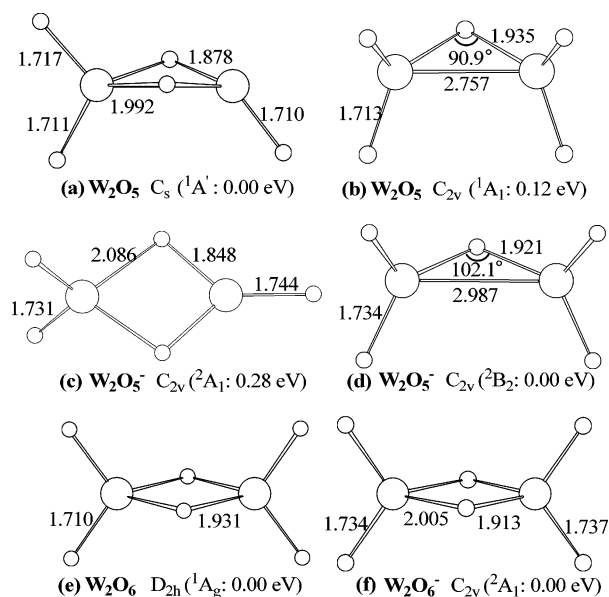


Figure 12. Optimized structures and their relative energies for W_2O_n and W_2O_n^- ($n = 5, 6$). The bond lengths are in Å.

atoms and the other W atom is only bonded to one terminal O atom. An isomer with C_{2v} symmetry (1A_1) and a single-bridging O atom is only 0.12 eV higher in energy (Figure 12b), which is similar to the structure identified by Sun et al.³⁰ The ground state of W_2O_5^- is identified as C_{2v} (2B_2) (Figure 12d), which is related to the C_{2v} (1A_1) isomer of neutral W_2O_5 . The dibridged structure, C_{2v} (2A_1), which is similar to the neutral ground state, is 0.28 eV higher in energy (Figure 12c).

4.6. W_2O_6 and W_2O_6^- . The ground-state structures of W_2O_6 and W_2O_6^- are also shown in Figure 12. The ground state of

W_2O_6 neutral is D_{2h} (1A_g) (Figure 12e), in agreement with that found by Sun et al.³⁰ This structure can be viewed as two tetrahedral WO_4 sharing an edge. The global minimum of W_2O_6^- corresponds to a C_{2v} (2A_1) structure (Figure 12f), in which the rhombus W_2O_2 unit is distorted relative to the neutral, suggesting that the extra electron is localized on one W atom in the anion. The corresponding D_{2h} structure of W_2O_6^- is a transition state with a low imaginary vibrational frequency ($173.3i \text{ cm}^{-1}$) in our calculations.

5. Discussion

To date, there are very few published experimental^{25–30} and computational³⁰ studies of W_2O_n^- or W_2O_n . Tungsten is a group VIB element with an electron configuration of $5d^46s^2$. It is capable of forming W–W multiple bond in its dimer, whose bond energy was estimated to be $5 \pm 1 \text{ eV}$.⁵⁶ Tungsten forms two principal oxides in the bulk:⁵⁷ WO_3 and WO_2 , in which W assumes formal oxidation states of +6 and +4, respectively. The W=O double bond is very strong with a bond energy of 6.96 eV,⁵⁸ which is important to understand the structures of the tungsten oxide clusters. Our previous work on the mono-tungsten oxide clusters showed that W prefers tetrahedral coordination with O,²³ as it does in aqueous solutions,⁵⁷ in crystalline salts such as Na_2WO_4 , CaWO_4 , and $\text{Al}_2(\text{WO}_4)_3$,^{59–61} and on tungsten oxide catalytic surfaces.^{4–9} The electronic structures of tungsten oxide clusters are rather complicated, in particular for the oxygen-deficient clusters due to the W 5d electrons, and are challenging computationally. In the current study, we will combine the experimental PES data and the DFT results to establish a coherent picture for the electronic structure evolution in W_2O_n^- and W_2O_n clusters and to elucidate the chemical bonding in these systems.

5.1. Comparison between Calculations and Experiments and Interpretation of the Photoelectron Spectra. In the single particle picture, photodetachment involves removal of electrons from occupied molecular orbitals (MOs) of an anion. The final states are the ground and excited states of the corresponding neutral. The lowest binding energy band in a PES spectrum involves photodetachment transition from the ground state of the anion to that of the neutral. The differences between the higher binding energy bands and the lowest binding energy band in the PES spectrum represent the excitation energies of the neutral cluster. To facilitate direct comparison between theory and experiment, we calculated the vertical excitation energies of W_2O_n on the basis of the identified anion ground-state structures. In Figure 7, the experimental PES spectra of the whole W_2O_n^- ($n = 1–6$) series are compared with the simulated spectra, which are generated by convoluting a Gaussian to each vertical detachment energy. All the calculated VDEs are collected in Table 2 along with the experimental data. Within the single electron picture, each singly occupied MO of the anion will generate a single PES band with the associated vibrational structures governed by the Franck–Condon principle, whereas a doubly occupied MO for an open-shell anion will result in two detachment channels because of the removal of either the spin-down (β) or the spin-up (α) electron. The β channels, leading to higher spin multiplicities in an open-shell anion, usually dominate the PES spectra because they have higher detachment cross sections than the α channels. In particular, when the PES spectra appear congested or continuous, the α channels are more likely to be buried. Therefore, except for the few α channels from singly occupied MOs, all the β channels listed in the left column in the theoretical VDEs in Table 2 should be considered as major contributors to the experimental

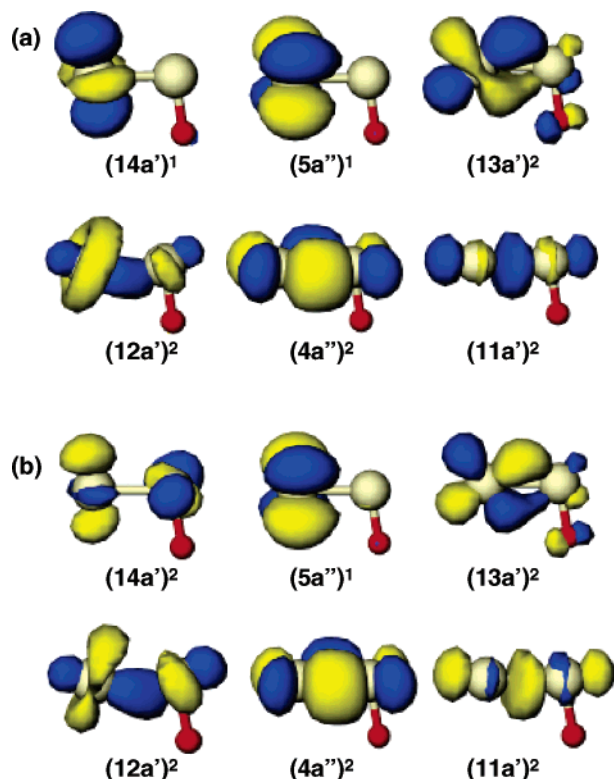


Figure 13. Molecular orbital pictures of (a) W_2O and (b) W_2O^- .

PES spectra. In the following, we will attempt to qualitatively account for the observed PES features using the DFT results. Considering the complicated nature of the electronic structures of these systems, many of the assignments should be considered tentative.

5.1.1. W_2O and W_2O^- . The ground state of W_2O is open-shell with C_s ($^3A''$) symmetry and a valent electronic configuration $(11a')^2(4a'')^2(12a')^2(13a')^2(5a'')^1(14a')^1$. The MO pictures are shown in Figure 13a. The $11a'$ MO corresponds to a σ bond mainly from the W d_z orbitals (mixed with some s component), the $4a''$ and $13a'$ MOs are two π bonds, and the $12a'$ MO corresponds to a σ bond mainly from the W s orbitals (mixed with some d_{z^2} component). The two singly occupied $5a''$ and $14a'$ MOs are nonbonding 5d orbitals, where the two unpaired electrons are situated on the same tungsten atom that is not bonded to the O atom. In the ground state of W_2O^- , the extra electron enters the $14a'$ MO, resulting in a C_s $^2A''$ state with an electronic configuration $(11a')^2(4a'')^2(12a')^2(13a')^2(5a'')^1(14a')^2$. The corresponding MO pictures are shown in Figure 13b. Spin density calculations show that the extra electron is situated on the W atom that is not bonded to the terminal oxygen atom.

Electron detachment from the doubly occupied $14a'$ HOMO of the anion will generate a triplet and a singlet neutral state, whose VDEs were calculated to be 1.24 and 1.63 eV, respectively. The triplet state corresponds to the neutral ground state and should be compared with the observed ground-state transition X (VDE: 1.61 eV); the singlet state should be compared to band A (VDE: 2.06 eV) in the PES spectra (Figure 1, Table 2). The similar band shape and vibrational frequencies observed for these two bands provide additional experimental support for these assignments. However, the VDEs of these two transitions are underestimated by ~ 0.4 eV in the current calculations, most likely because of the neglect of the spin-orbit coupling. The next detachment channel is from the singly occupied $5a''$ MO with a calculated VDE of 1.78 eV, which should correspond to band B (VDE: 2.25 eV) in the PES

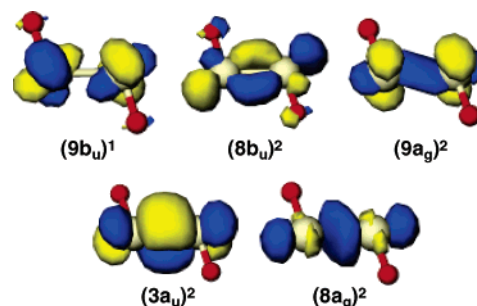


Figure 14. Molecular orbital pictures of W_2O_2^- .

spectra. Again, the calculated VDE is off by ~ 0.4 eV for this detachment channel. The higher binding energy part of the PES spectra is highly congested and not very well resolved (Figure 1). Our calculations showed eight detachment channels from the $13a'$, $12a'$, $4a''$, and $11a'$ MOs in this part of the spectra (Table 2), all being bonding orbitals due to the 5d electrons, consistent with the complexity of the observed PES spectra. The observed short vibrational progressions of features X and A are consistent with the nonbonding nature of the corresponding $14a'$ MO. The very sharp peak B agrees with the fact that the $5a''$ MO is a pure W 5d orbital (Figure 13). In contrast, the higher binding energy bands which originate from the strong W–W bonding MOs are much broader.

5.1.2. W_2O_2 and W_2O_2^- . The ground state of W_2O_2 is closed shell with C_{2h} (1A_g) symmetry and a valent electronic configuration of $(7a_g)^2(2a_u)^2(8a_g)^2(3a_u)^2(9a_g)^2(8b_u)^2(9b_u)^0$. The $9b_u$ orbital is the LUMO, which is an antibonding δ^* orbital and singly occupied in the W_2O_2^- anion. The MO pictures are shown in Figure 14. In the W_2O_2 neutral, eight W 5d electrons occupy four bonding orbitals: one σ bond ($8a_g$), two π bonds ($3a_u$ and $8b_u$), and one δ bond ($9a_g$), giving rise to a W–W bond order of four in W_2O_2 .

Photodetachment from the singly occupied $9b_u$ orbital leads to the neutral ground state with a calculated VDE of 2.04 eV (Table 2), which is in reasonable agreement with the experimental VDE for the ground-state PES band of 1.81 eV. The next detachment channel is from the $8b_u$ orbital, resulting in a triplet and singlet final state with calculated VDEs at 2.30 and 2.84 eV (Table 2), respectively. These calculated VDEs compared well with the VDEs of bands A (2.29 eV) and B (2.54 eV) in the PES spectra (Figure 2). Band C (VDE: 2.69 eV) in the PES spectra should be due to detachment from the $9a_g(\beta)$ with a calculated VDE of 2.88 eV. The calculated VDE from the $9a_g(\alpha)$ is quite high at 4.16 eV. The calculated VDEs for detachments from the $3a_u$ orbital are also relatively high, 3.80 and 4.22 eV for the triplet and singlet final states, respectively. These three detachment channels probably correspond to the broad features above 3.5 eV (E and F) in the PES spectrum (Figure 2c). No theoretical detachment channels were predicted at ~ 3.2 eV in the D band region (Figure 2). The intensity of band D is relatively weak and it may be due to multielectron processes. In the simulated PES spectrum for W_2O_2^- shown in Figure 7, several higher binding energy features beyond the experimental spectral range are also shown. Overall, the calculated VDE pattern is in good agreement with the PES spectra.

5.1.3. W_2O_3 and W_2O_3^- . The ground state of W_2O_3 is a closed-shell C_{2v} (1A_1) species with a valent electronic configuration of $(10a_1)^2(3b_2)^2(8b_1)^2(11a_1)^2(4b_2)^2(12a_1)^2$. W_2O_3^- is C_{2v} (2B_1) with a valent configuration of $(10a_1)^2(3b_2)^2(8b_1)^2(11a_1)^2(4b_2)^2(12a_1)^2(9b_1)^1$, in which the extra electron occupies the $9b_1$

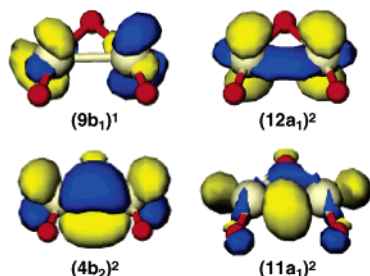


Figure 15. Molecular orbital pictures of $W_2O_3^-$.

LUMO of neutral W_2O_3 . The top few MOs mainly derived from the W 5d orbitals are shown in Figure 15. Neutral W_2O_3 still possesses a W–W triple bond because of the strong d–d bonding characters in the $11a_1$, $4b_2$, and $12a_1$ MOs. The $9b_1$ LUMO is an antibonding δ^* orbital. Spin density calculations indicated that the extra electron in $W_2O_3^-$ is shared by the two tungsten atoms, giving rise to the C_{2v} symmetry in the $W_2O_3^-$ anion.

The first PES band of $W_2O_3^-$ is very sharp, indicating that there is little structural change between the ground state of the anion and the corresponding neutral state. The similar structures between the C_{2v} (2B_1) ground state of $W_2O_3^-$ (Figure 10e) and the C_{2v} (1A_1) species of W_2O_3 are in excellent agreement with the sharp PES feature. The very weak vibrational excitation in the W–O stretching mode in the X band (Figure 3a) is also consistent with the very small terminal W–O bond length change between the C_{2v} $W_2O_3^-$ and W_2O_3 . The calculated VDE for detachment from the $9b_1$ MO is 2.50 eV, also in very good agreement with the experimental VDE for the ground-state transition (2.25 eV), as given in Table 2. The sharp peak A (VDE: 2.88 eV) in the PES spectra should correspond to detachment from the $12a_1(\beta)$ orbital with a calculated VDE of 3.03 eV. The calculated VDE for the corresponding singlet state for detachment from the $12a_1(\alpha)$ MO is 4.26 eV, which falls in the spectral range between 3.5 and 5 eV. In this spectral range, three broad bands (B, C, D) are observed, which should also contain four detachment transitions from the $4b_2$ and $11a_1$ MOs. The calculated VDEs for these four channels range from 3.65 to 4.91 eV (Table 2), in very good agreement with the PES data. The higher binding energy features above 5.5 eV in the PES spectra (Figure 3) are due to detachment from O 2p-based MOs. VDEs for three such orbitals were calculated as shown in Table 2. The first O 2p-based MO is the $8b_1(\beta)$ MO with a calculated VDE of 5.74 eV, in good agreement with onset of O 2p features observed in the PES spectra (Figures 3 and 7). Overall, the calculated VDE pattern from the C_{2v} $W_2O_3^-$ is in excellent agreement with the experimental PES data, as shown in Table 2 and Figure 7.

5.1.4. W_2O_4 and $W_2O_4^-$. The W_2O_4 and $W_2O_4^-$ species represent the most complicated systems in our current calculations. There seems to be a competition between the W–W bonding and W–O bonding and between the W–O single bonds and W=O double bonds. The two low-lying structures of W_2O_4 (Figure 11a, b) have very different W–O connectivities, but they are nearly degenerate and both are triplet with two unpaired spins. The current calculations cannot distinguish which one should be the ground state. The W–W distance is about the same in both structures, and they each can be viewed to have a W–W single bond. However, the dibridged structure only has two terminal O atoms (W=O bonds), whereas the monobridged structure has three terminal O atoms (W=O bonds). Thus, it appears that one W=O double bond is about equivalent to two W–O single bonds in the bridging position. Interestingly,

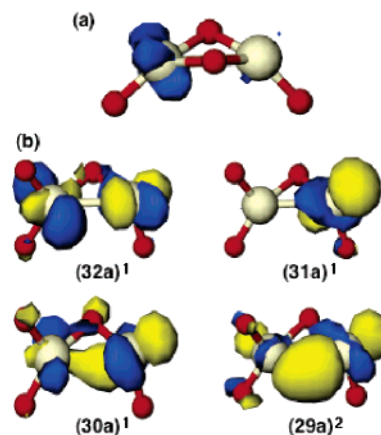


Figure 16. (a) Spin densities of the W_2O_4 neutral and (b) molecular orbital pictures of the $W_2O_4^-$ anion.

the W–O distances in the four-membered ring of the dibridged structure are different with two long W–O distances (2.04 Å) and two short W–O distances (1.85 Å). Thus, this isomer can also be viewed as a W=O unit interacting with a stable WO_3 unit. Indeed, the spin densities in this structure are mainly localized on the W atom of the W=O unit, as shown in Figure 16a.

In the $W_2O_4^-$ anion, the monobridged structure with a quartet state (C_1 , 4A) becomes the ground state (Figure 11e). The monobridged doublet state (Figure 11f) is higher in energy by 0.18 eV, but the quartet dibridged structure is higher in energy by 0.27 eV (Figure 11g). Thus, we will use the lowest energy quartet monobridged $W_2O_4^-$ structure to interpret the PES spectra. This isomer has an electron configuration of $(25a)^2(26a)^2(27a)^2(28a)^2(29a)^2(30a)^1(31a)^1(32a)^1$. The top four predominantly 5d-type MOs are shown in Figure 16b. The $32a$ MO is a W–W antibonding orbital. Thus, detachment from the $32a$ orbital results in a significant decrease in the W–W distance in the neutral cluster (Figure 11b). The calculated VDE is 3.23 eV (Table 2), in very good agreement with the experimental VDE of the X band (3.13 eV). The $31a$ MO is a nonbonding d orbital (Figure 16b) with a calculated VDE of 4.33 eV, which is to be compared to the A band in the PES spectra (VDE: 3.90 eV). The band B (VDE: 4.20 eV) should correspond to detachment from the weakly bonding $30a$ orbital with a calculated VDE of 4.59 eV. The weak band C at 5.0 eV in the PES spectra (Figure 4) should correspond to detachment from the $29a$ orbital. Our calculation yielded a VDE of ~ 5 eV but showed strong multireference character for this detachment channel, in agreement with the weak intensity of this band. The closely lying O 2p type orbitals start from $28a$. The calculated VDEs for these detachment channels are in good agreement with the observed PES spectra (Table 2, Figure 7). In particular, the onset of the O 2p type MO ($28a$) has a calculated VDE of 6.02 eV, in excellent agreement with the observed band D (VDE: ~ 6.0 eV).

5.1.5. W_2O_5 and $W_2O_5^-$. The ground state of W_2O_5 is the dibridged C_s structure (Figure 12a). The monobridged C_{2v} structure (Figure 12b) is only 0.12 eV higher in energy. There seems to be a competition between W–W and W–O bonding. In the C_s structure, there is no W–W bonding and the extra pair of d-electrons is essentially a lone pair localized on the tricoordinated W atom (Figure 17a). On the other hand, there is a W–W bond in the C_{2v} structure, as evidenced from its HOMO ($12a_1$), which has strong d–d bonding character. In the anion, the monobridged C_{2v} structure (Figure 12d) becomes the ground state with a valent electronic configuration

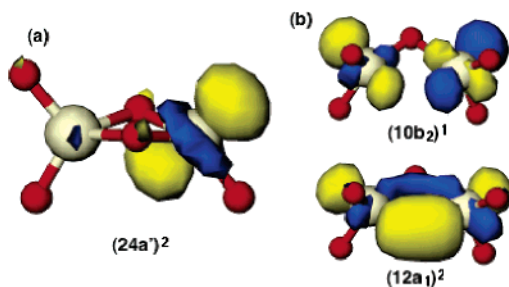


Figure 17. (a) HOMO picture of the W_2O_5 neutral and (b) molecular orbitals of the $W_2O_5^-$ anion.

of $(10a_1)^2(8b_2)^2(6b_1)^2(11a_1)^2(9b_2)^2(7b_1)^2(6a_2)^2(12a_1)^2(10b_2)^1$, where the extra electron enters the $10b_2$ orbital with d–d antibonding character (Figure 17b), the $12a_1$ MO is the d–d bonding orbital, and all MOs from $6a_2$ and below are of O 2p character.

Photodetachment from the singly occupied $10b_2$ orbital of $W_2O_5^-$ yields the first PES band X (VDE: 3.66 eV), which compares well with the calculated VDE of 3.88 eV (Table 2). The next detachment channel is from $12a_1(\beta)$ with a calculated VDE of 4.73 eV, in excellent agreement with band A (VDE: 4.79 eV). The calculated VDE from $12a_1(\alpha)$ is 6.66 eV, which falls in the spectral region where detachments from O 2p-based MOs dominate. The first detachment channel from an O 2p-based MO ($6a_2$) has a calculated VDE of 6.51 eV, in excellent agreement with observed band B (VDE: 6.45 eV). The congested spectral features above 6 eV in Figure 5 can all be attributed to detachments from O 2p-based MOs with a contribution from $12a_1(\alpha)$, as given in Table 2 and shown in Figure 7. Overall, the calculated VDEs from the $W_2O_5^-$ anion ground state are in excellent agreement with the observed PES spectra.

5.1.6. W_2O_6 and $W_2O_6^-$. W_2O_6 is a stoichiometric molecule, in which each W achieves its favorite oxidation state W^{6+} , that is, all the valence electrons of W are used to form bonds with the O atoms. The observed PES spectra of $W_2O_6^-$ (Figure 6) is consistent with a stable neutral cluster with a large HOMO–LUMO gap (2.8 eV). Sun et al. previously reported a PES spectrum of $W_2O_6^-$ at 193 nm,³⁰ which is consistent with the current data at the same wavelength (Figure 6b). However, as shown in Figure 6, the 193-nm photon does not allow the first excited state to be fully observed. Consequently, the HOMO–LUMO gap estimated by Sun et al. (2.5 eV) was lower than the true value. In addition, the current vibrationally resolved data at 266 nm (Figure 6a) yields a much more accurate ADE (3.52 eV), compared to a lower value of 3.40 eV reported by Sun et al. Previous PES works by us and Gantefor et al. revealed an energy gap of 1.40 eV for the stoichiometric WO_3 monomer.^{23,62} Interestingly, the 2.8 eV HOMO–LUMO gap of the W_2O_6 dimer is already rather close to the energy gaps of bulk WO_3 (indirect gap, ~ 2.6 eV; direct gap, ~ 3.5 – 3.7 eV).⁶³

The ground-state structure that we obtained for W_2O_6 is D_{2h} (Figure 12e), in agreement with that reported by Sun et al.³⁰ This structure can be viewed as the fusion of two tetrahedral WO_4 units. In the anion, the extra electron enters the $17a_1$ LUMO of W_2O_6 with mainly 5d character. However, as shown in Figure 18, the extra electron is not shared equally by the two W atoms, and it can be viewed as mainly localized on one side of the molecule. Thus, the ground state of $W_2O_6^-$ has a lower symmetry C_{2v} structure (Figure 12f) with a valent electron configuration of $(7b_1)^2(16a_1)^2(3a_2)^2(8b_1)^2(10b_2)^2(11b_2)^2(17a_1)^1$. All the MOs except $17a_1$ are of O 2p character. The calculated VDE from detachment from the $17a_1$ orbital was 3.71 eV, in excellent agreement with the experimental ground-state feature

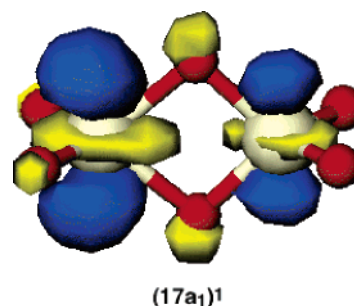


Figure 18. The HOMO picture of the $W_2O_6^-$ anion.

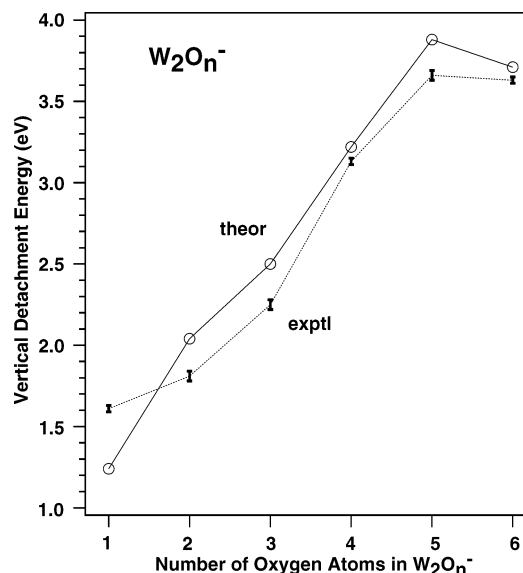


Figure 19. Measured vertical detachment energies (dashed line with error bars) versus the number of oxygen atoms in $W_2O_n^-$. Those from DFT calculations (circles) are also shown for comparison.

X (VDE: 3.63 eV). The next detachment channel is from $11b_2(\beta)$ with a calculated VDE of 6.43 eV, compared very well with the VDE of the A band (6.57 eV). The calculated energy gap (2.72 eV) is also consistent with the measured value of 2.8 eV. The calculated VDEs from higher binding energy detachment channels are also in excellent agreement with the experimental data (Table 2 and Figure 7). The observed vibrational progression (Figure 6a) primarily consists of W–O stretching, but other low-frequency modes must also be involved because the observed spectrum appears to be more complicated in the high binding energy side. This observation provides additional evidence for the geometrical changes between the ground states of $W_2O_6^-$ and W_2O_6 .

5.2. Sequential Oxidation and Spectral Evolution. Figure 19 shows the observed VDE as a function of oxygen content in the $W_2O_n^-$ clusters, as well as the calculated VDEs. The electron binding energy is observed to increase monotonically as a function of oxygen from $n = 1$ – 5 , clearly showing a behavior of sequential oxidation of the W_2 dimer. The slight decrease of electron binding energies in $W_2O_6^-$ relative to $W_2O_5^-$ is due to the stability of W_2O_6 as a neutral molecule and its large HOMO–LUMO gap, which significantly destabilizes the LUMO level. The behavior of sequential oxidation was first observed in $Fe_xO_y^-$ clusters^{31,32} and $Al_3O_n^-$ clusters,³⁵ which are more ionic systems, and is due to the high electron affinity of the O atom and to charge transfers from the metal center to oxygen. The O atoms in the oxide clusters can be viewed to be O^{2-} units formally, which have much higher electron binding energies (> 5 eV), whereas metallic electrons usually have lower

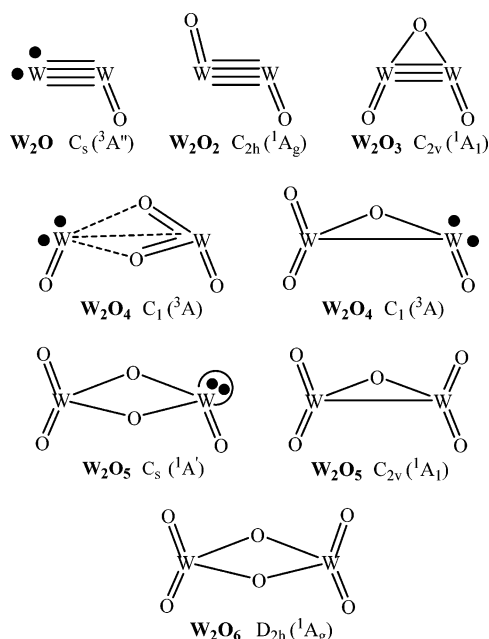


Figure 20. Valence-bond descriptions of W_2O_n ($n = 1-6$). Bond orders, unpaired electrons, and lone pair are indicated. For W_2O_4 and W_2O_5 , two competing structures are shown.

electron binding energies. However, as the number of O atoms increases, the W atoms become more positively charged, stabilizing the remaining d electrons and increasing their binding energies. Although the W–O bonding has significant covalent character, the sequential oxidation behavior in $W_2O_n^-$ clusters is clearly observed in the electron binding energy trend. Sequential oxidation in $W_4O_n^-$ clusters have also been observed recently.⁶⁴

The behavior of sequential oxidation is also clearly shown in the PES spectral features. In Figure 7, the PES spectra of all $W_2O_n^-$ are shown and compared. The lower binding energy features labeled “d” are all due to W 5d electrons, as discussed above and shown in the MOs of Figures 13–18. As the oxygen content increases, the number of 5d features decrease because of the transfer of electrons from W to O and the formation of W–O bonds. In the stoichiometric W_2O_6 molecule, all the d electrons are transferred from W to O and W achieves its highest oxidation state of 6+. The O 2p-derived features all have very high binding energies (>5.5 eV), labeled as “p” in Figure 7. For W_2O^- and $W_2O_2^-$, the densities of states derived from the O 2p features are relatively low. Thus, the high binding energy part of the spectra at 193 and 157 nm (not shown) has very low signal levels and is very noisy. For the larger cluster starting at $W_2O_3^-$, the O 2p features dominate the high binding energy part of the spectra (Figure 7).

5.3. Chemical Bonding in W_2O_n ($n = 1-6$). The MOs presented in Figures 13–18 also provide insight into the nature of the chemical bonding in W_2O_n ($n = 1-6$) and allow a more detailed understanding about the behavior of sequential oxidation as a function of oxygen content, as schematically shown in the valence-bond descriptions of W_2O_n in Figure 20. Bare W_2 has a formal bond order of six with an electron configuration of $\pi^4\sigma_d-d^2\sigma_s-s^2\delta^4$, in which all the 12 valence electrons of the two W atoms occupy bonding MOs, although the δ bonds are relatively weak and close to be nonbonding. Indeed, the W_2 dimer is known to have a very high dissociation energy (5 eV), consistent with its multiple bonds.⁵⁶ Multiply bonded ditungsten units are also well established in inorganic chemistry.⁶⁵

In W_2O (Figures 8a and 13a), the oxygen atom breaks the two weak δ bonds while forming a $W=O$ double bond, resulting in two half-filled nonbonding MOs ($14a'$ and $5a''$) localized on one W atom. The two σ and the two π bonds are nearly unaffected in W_2O , which can thus be characterized to possess a quadruple W–W bond with diradical character (Figure 20). W_2O can readily accept another O atom to form a $W=O$ double bond using the two unpaired electrons, leaving essentially the W–W quadruple bond intact (Figure 20). This is indeed the case, as can be seen by the similar W–W bond length and $\angle O-W-W$ bond angle in the two clusters. The structures with bridging O are less stable in both W_2O and W_2O_2 . This is attributed to the strength of the $W=O$ double bond, and it is also because the short W–W distance makes it unfavorable for the bridging O due to the sharp $\angle W-O-W$ angle.

Further oxidation breaks the $8b_u$ π bond in W_2O_2 , resulting in a W–W bond order of three in W_2O_3 , in which the additional O atom assumes a bridging position. It seems that the relative positions of the bridging O and the two terminal O atoms are flexible, resulting in three nearly degenerate isomers (Figure 10a, b, c). However, the nonbridging isomer (Figure 10d) is less stable because of the significant weakening of the W–W bonding. The potential energy surfaces of W_2O_4 become much more complicated, and two very different structures are competitive to be the ground state, that is, the dibridged isomer and the monobridged isomer. In either structure, only a single W–W bond exists because of the two unpaired spins, which tend to localize on one W. Additionally, the dibridged isomer can be viewed as a $W=O$ unit interacting with a WO_3 unit because the two bridging W–O distances are different. For W_2O_5 , there are also two competitive low-lying structures, which are related to the two low-lying structures of W_2O_4 . However, in the monobridged W_2O_5 structure (Figure 12b), there is a single W–W bond, whereas in the dibridged structure there is no significant W–W bonding because the two d electrons form essentially a lone pair localized on one W site. Addition of an O atom to either isomers of W_2O_5 leads to the stoichiometric and classical dibridged structure of W_2O_6 , which can be considered to be a fusion of two tetrahedral WO_4 units. In W_2O_6 , all the 12 valence electrons on the two W atoms are used to form W–O bonds, resulting in a stable molecule with a large HOMO–LUMO gap.

Thus, we see a clear trend of sequential oxidation of the W_2 dimer in W_2O_n from $n = 1$ to 6. The strong sextuple bond in W_2 is sequentially broken with the formation of W–O bonds, accompanied by the transfer of two electrons from W to O. The PES spectra provide a vivid picture for this sequential oxidation. With increasing O content, the low binding energy features derived from W systematically diminish, which emerge as O 2p-based bands at rather high binding energies (above 5.5 eV). Thus, the electronic structure of the W_2O_n species become simpler as the size increases because of the loss of d electrons.

6. Conclusions

We report a systematic photoelectron spectroscopy and density functional study of a series of ditungsten oxide clusters: $W_2O_n^-$ and W_2O_n ($n = 1-6$). Well-resolved photoelectron spectra were obtained at several photon energies, yielding a wealth of electronic structure information. Upon increasing the oxygen content in $W_2O_n^-$, the low binding energy W 5d-based features are diminishing in numbers, and simultaneously the whole spectrum is gradually shifting to higher binding energies. A behavior of sequential oxidation as a result

of charge transfers from W to O was therefore observed. The photoelectron spectra of $W_2O_6^-$ show a large energy gap of 2.8 eV, characteristic of a stable stoichiometric W_2O_6 neutral molecule with a large HOMO–LUMO gap. Extensive density functional calculations were carried out and combined with the experimental data to elucidate the structure and chemical bonding in the W_2O_n clusters. Oxygen-deficient clusters create lone pairs or unpaired electrons on W centers, making them much more reactive. Such defect sites are likely active sites in the bulk oxide or on surfaces. Although the W_2O_n clusters may not be large enough to simulate the bulk coordination environment, it is hoped that continued studies of larger W_xO_y clusters will uncover appropriate models for the bulk defect sites and provide insight into their electronic and chemical properties.

Acknowledgment. We thank Dr. B. Kiran for valuable discussions. This work was supported by the Chemical Sciences, Geosciences and Biosciences Division, Office of Basic Energy Sciences, U.S. Department of Energy (DOE) under grant No. DE-FG02-03ER15481 (catalysis center program) and was performed at the W. R. Wiley Environmental Molecular Sciences Laboratory (EMSL), a national scientific user facility sponsored by DOE's Office of Biological and Environmental Research and located at Pacific Northwest National Laboratory, operated for DOE by Battelle. All calculations were done using the EMSL Molecular Science Computing Facility.

References and Notes

- Granqvist, C. G. *Sol. Energy Mater. Sol. Cells* **2000**, 60, 201.
- Manno, D.; Serra, A.; Giulio, M. D.; Micocci, G.; Tepore, A. *Thin Solid Films* **1998**, 324, 44.
- Moulzolf, S. C.; LeGore, L. J.; Lad, R. J. *Thin Solid Films* **2001**, 400, 56.
- Salvatl, L., Jr.; Makovsky, L. E.; Stencel, J. M.; Brown, F. R.; Hercules, D. M. *J. Phys. Chem.* **1981**, 85, 3700.
- Horsley, J. A.; Wachs, I. E.; Brown, J. M.; Via, G. H.; Hardcastle, F. D. *J. Phys. Chem.* **1987**, 91, 4014.
- Gazzoli, D.; Valigi, M.; Dragone, R.; Marucci, A.; Mattei, G. *J. Phys. Chem. B* **1997**, 101, 11129.
- Bige, C.; Hilaire, L.; Maire, G. *J. Catal.* **2001**, 198, 208.
- Ji, S. F.; Xiao, T. C.; Li, S. B.; Xu, C. Z.; Hou, R. L.; Coleman, K. S.; Green, M. L. H. *Appl. Catal. A* **2002**, 225, 271.
- Mamede, A. S.; Payen, E.; Grange, P.; Poncelet, G.; Ion, A.; Alifanti, M.; Parvulescu, V. I. *J. Catal.* **2004**, 223, 1.
- For a recent feature article, see: Zemski, K. A.; Justes, D. R.; Castleman, A. W., Jr. *J. Phys. Chem. B* **2002**, 106, 6136.
- Fialko, E. F.; Kirkhtenko, A. V.; Goncharov, V. B.; Zamaraev, K. I. *J. Phys. Chem. B* **1997**, 101, 5772.
- Shi, Y.; Ervin, K. M. *J. Chem. Phys.* **1998**, 108, 1757.
- Sanchez, A.; Abbet, S.; Heiz, U.; Schneider, W. D.; Hakkinen, H.; Barnett, R. N.; Landman, U. *J. Phys. Chem. A* **1999**, 103, 9573.
- Jackson, P.; Fisher, K. J.; Willett, G. D. *Chem. Phys.* **2000**, 262, 179.
- Wallace, W. T.; Whetten, R. L. *J. Am. Chem. Soc.* **2002**, 124, 7499.
- Asmis, K. R.; Brummer, M.; Kaposta, C.; Snatambrogio, G.; von Helden, G.; Meijer, G.; Rademann, K.; Woste, L. *Phys. Chem. Chem. Phys.* **2002**, 4, 1101.
- Socaciu, L. D.; Hagen, J.; Bernhardt, T. M.; Woste, L.; Heiz, U.; Hakkinen, H.; Landman, U. *J. Am. Chem. Soc.* **2003**, 125, 10437.
- Baltea, I.; Balaj, O. P.; Fox, B. S.; Beyer, M. K.; Bastl, Z.; Bondybey, V. E. *Phys. Chem. Chem. Phys.* **2003**, 5, 1213.
- Stolcic, D.; Fischer, M.; Gantefor, G.; Kim, Y. D.; Sun, Q.; Jena, P. *J. Am. Chem. Soc.* **2003**, 125, 2848.
- Waters, T.; O'Hair, R. A.; Wedd, A. G. *J. Am. Chem. Soc.* **2003**, 125, 3384.
- Justes, D. R.; Mitric, R.; Moore, N. A.; Bonacic-Koutecky, V.; Castleman, A. W., Jr. *J. Am. Chem. Soc.* **2003**, 125, 6289.
- Yoder, B. L.; Maze, J. T.; Raghavachari, K.; Jarrold, C. C. *J. Chem. Phys.* **2005**, 122, 094313.
- Zhai, H. J.; Kiran, B.; Cui, L. F.; Li, X.; Dixon, D. A.; Wang, L. S. *J. Am. Chem. Soc.* **2004**, 126, 16134.
- Zhai, H. J.; Wang, L. S. *J. Chem. Phys.* **2005**, 122, 051101.
- Ackermann, R. J.; Rauh, E. G. *J. Phys. Chem.* **1963**, 67, 2596.
- Weltner, W., Jr.; McLeod, D., Jr. *J. Mol. Spectrosc.* **1965**, 17, 276.
- Bare, W. D.; Souter, P. F.; Andrews, L. *J. Phys. Chem. A* **1998**, 102, 8279.
- Maleknia, S.; Brodbelt, J.; Pope, K. *J. Am. Soc. Mass Spectrom.* **1991**, 2, 212.
- Aubriet, F.; Muller, J. F. *J. Phys. Chem. A* **2002**, 106, 6053.
- Sun, Q.; Rao, B. K.; Jena, P.; Stolcic, D.; Kim, Y. D.; Gantefor, G.; Castleman, A. W., Jr. *J. Chem. Phys.* **2004**, 121, 9417.
- Wang, L. S.; Wu, H.; Desai, S. R. *Phys. Rev. Lett.* **1996**, 76, 4853.
- Wu, H.; Desai, S. R.; Wang, L. S. *J. Am. Chem. Soc.* **1996**, 118, 5296.
- Wang, L. S.; Wu, H.; Desai, S. R.; Lou, L. *Phys. Rev. B* **1996**, 53, 8028.
- Wu, H.; Wang, L. S. *J. Chem. Phys.* **1997**, 107, 8221.
- Wu, H.; Li, X.; Wang, X. B.; Ding, C. F.; Wang, L. S. *J. Chem. Phys.* **1998**, 109, 449.
- Wang, L. S. Photodetachment Photoelectron Spectroscopy of Transition Metal Oxide Species. In *Advanced Series in Physical Chemistry*, Vol. 10. Photoionization and Photodetachment; Ng, C. Y., Ed.; World Scientific: Singapore, 2000; pp 854–957.
- Gustev, G. L.; Jena, P.; Zhai, H. J.; Wang, L. S. *J. Chem. Phys.* **2001**, 115, 7935.
- Zhai, H. J.; Wang, L. S. *J. Chem. Phys.* **2002**, 117, 7882.
- Wang, L. S.; Cheng, H. S.; Fan, J. J. *J. Chem. Phys.* **1995**, 102, 9480.
- Wang, L. S.; Wu, H. In *Advances in Metal and Semiconductor Clusters. IV. Cluster Materials*; Duncan, M. A., Ed.; JAI: Greenwich, CT, 1998; pp 299–343.
- Becke, A. D. *J. Chem. Phys.* **1993**, 98, 1372/5648.
- Lee, C.; Yang, W.; Parr, R. G. *Phys. Rev. B* **1988**, 37, 785.
- Stephens, P. J.; Devlin, F. J.; Chabalowski, C. F.; Frisch, M. J. *J. Phys. Chem.* **1994**, 98, 11623.
- Andrae, A.; Haeussermann, U.; Dolg, M.; Stoll, H.; Preuss, H. *Theor. Chim. Acta* **1990**, 77, 123.
- Kuchle, W.; Dolg, M.; Stoll, H.; Preuss, H. *Pseudopotentials of the Stuttgart/Dresden Group 1998*, Revision Aug 11, 1998 (<http://www.theochem.uni-stuttgart.de/pseudopotentials>).
- Martin, J. M. L.; Sundermann, A. *J. Chem. Phys.* **2001**, 114, 3408.
- Dunning, T. H., Jr. *J. Chem. Phys.* **1989**, 90, 1007.
- Kendall, R. A.; Dunning, T. H., Jr.; Harrison, R. J. *J. Chem. Phys.* **1992**, 96, 6796.
- Yang, Y.; Waters, T.; Wang, X. B.; O'Hair, R. A. J.; Wedd, A. G.; Dixon, D. A.; Li, J.; Wang, L. S. *J. Phys. Chem. A* **2004**, 108, 10089.
- Li, J.; Li, X.; Zhai, H. J.; Wang, L. S. *Science* **2003**, 299, 864.
- Li, X.; Kiran, B.; Li, J.; Zhai, H. J.; Wang, L. S. *Angew. Chem., Int. Ed.* **2002**, 41, 4786.
- Straatsma, T. P.; Apra, E.; Windus, T. L. et al. *NWChem, A Computational Chemistry Package for Parallel Computers, Version 4.6*; Pacific Northwest National Laboratory: Richland, WA, 2004.
- <http://ecce.emsl.pnl.gov/>.
- Wang, L. S.; Conceicao, J.; Jin, C.; Smalley, I. *Chem. Phys. Lett.* **1991**, 182, 5.
- Weidele, H.; Kreisle, D.; Recknagel, E.; Icking-Konert, G. S.; Handschuh, H.; Gantefor, G.; Eberhardt, W. *Chem. Phys. Lett.* **1995**, 237, 425.
- Morse, M. D. *Chem. Rev.* **1986**, 86, 1049.
- Greenwood N. N.; Earnshaw, A. *Chemistry of the Elements*; Butterworth-Heinemann: Oxford, U.K., 1998.
- Kerr, J. A. In *CRC Handbook of Chemistry and Physics*; Lide D. R., Ed.; CRC Press: Boca Raton, FL, 2000.
- Okada, K.; Morikawa, H.; Marumo, F.; Iwai, S. *Acta Crystallogr., Sect. B* **1974**, 30, 1872.
- Barker, A. S., Jr. *Phys. Rev. A* **1964**, 135, 742.
- Craig, D. C.; Stephenson, N. C. *Acta Crystallogr., Sect. B* **1968**, 24, 1250.
- Stolcic, D.; Kim, Y. D.; Gantefor, G. *J. Chem. Phys.* **2004**, 120, 5.
- Koffyberg, F. P.; Dwight, K.; Wold, A. *Solid State Commun.* **1979**, 30, 433.
- Sun, Q.; Rao, B. K.; Jena, P.; Stolcic, D.; Gantefor, G.; Kawazoe, Y. *Chem. Phys. Lett.* **2004**, 387, 29–34.
- Cotton, F. A.; Wilkinson, G. *Advance Inorganic Chemistry*, 5th ed.; Wiley: New York, 1988.